Radiation Performance Analysis of 28 GHz Antennas Integrated in 5G Mobile Terminal Housing

BO XU [1,2,3], **(Member, IEEE), ZHINONG YING**[4], **(Senior Member, IEEE), LUCIA SCIALACQUA**[5], **ALESSANDRO SCANNAVINI**[5], **LARS JACOB FOGED**[5], **(Senior Member, IEEE),** **THOMAS BOLIN**[4], **KUN ZHAO**[4,6], **SAILING HE**[1,2], **(Fellow, IEEE),** **AND MATS GUSTAFSSON** [7], **(Senior Member, IEEE)**

[1]Centre for Optical and Electromagnetic Research, Zhejiang University, Hangzhou 310058, China
[2]Department of Electromagnetic Engineering, KTH Royal Institute of Technology, SE-100 44 Stockholm, Sweden
[3]Ericsson Research, Ericsson AB, SE-164 80 Stockholm, Sweden
[4]Network Technology Lab, Research and Technology, Sony Mobile Communications AB, SE-221 88 Lund, Sweden
[5]Microwave Vision Italy, 00040 Pomezia, Italy
[6]Department of Electronic Systems, Antennas, Propagation and Radio Networking Section, Aalborg University, 9220 Alborg, Denmark
[7]Department of Electrical and Information Technology, Lund University, SE-221 00 Lund, Sweden

Corresponding author: Sailing He (sailing@jorcep.org)

ABSTRACT Radiation from printed millimeter-wave antennas integrated in mobile terminals is affected by surface currents on chassis, guided waves trapped in dielectric layers, superstrates, and the user's hand, making mobile antenna design for 5G communication challenging. In this paper, four canonical types of printed 28-GHz antenna elements are integrated in a 5G mobile terminal mock-up. Different kinds of terminal housing effects are examined separately, and the terminal housing effects are also diagnosed through equivalent currents by using the inverse source technique. To account for the terminal housing effects on a beam-scanning antenna subarray, we propose the effective beam-scanning efficiency to evaluate its coverage performance. This paper presents the detailed analysis, results, and new concepts regarding the terminal housing effects, and thereby provides valuable insight into the practical 5G mobile antenna design and radiation performance characterization.

INDEX TERMS 5G, effective beam-scanning efficiency, equivalent current, surface current, millimeter-wave antenna, mobile terminal, guided wave, user equipment, user's hand.

I. INTRODUCTION

Fifth-generation (5G) mobile communication is a timely topic in the telecommunication industry and in academia. Enhanced Mobile BroadBand (eMBB) as one of the three general usage scenarios supporting Gigabit-per-second data rate for 5G defined by International Telecommunication Union Radiocommunication Sector (ITU-R) in 2015, is now well-known in the telecommunication industry [1]. One of the key innovations to realize data rates up to 10 Gb/s and latency as low as 1 ms for eMBB is utilizing the millimeter-wave (mmWave) spectrum above 24 GHz, which contains a much larger available signal bandwidth compared to the current cellular spectrum [1]–[3]. In 2016, the U.S. Federal Communications Commission (FCC) and

the European Union (EU) allocated several 5G pioneer bands above 24 GHz [4], [5]. Two of these bands are close to or within the 28 GHz range: 27.5–28.35 GHz in the U.S. and 24.25–27.5 GHz in the EU. The first 5G commercial products are expected to be rolled out by 2020 [6].

Recently, many studies regarding 5G mmWave mobile antennas have been carried out. Different kinds of mmWave array antennas are developed for full-spherical coverage [7]–[12]. From the perspective of mobile antennas, user effects on mmWave channel modeling and radio link budgets were investigated [12]–[18]. References [19]–[25] studied human exposure to mmWave antennas operating in the immediate vicinity of human bodies. Various novel antenna designs for 5G mmWave mobile terminals were

proposed [26]–[31]. However, the previous works on 5G mobile antennas were restricted to antenna designs with chassis and their beam-scanning performance. There is a lack of literature investigating the mmWave antenna performance in mobile terminal housing environments (MTHE). In the mmWave bands, the dimensions of mobile terminals can be many wavelengths, while in the current 2G–4G cellular bands (700 MHz–6 GHz), the dimensions of mobile terminals are usually only around one half to a few wavelengths. In addition, the electrical thickness of dielectric layers is much larger for mmWave frequencies, and other components in mobile terminals become electrically large. Such changes in wavelength lead to significant impacts on design processes and radiation performance characterization of mmWave antennas integrated in 5G mobile terminals.

This paper comprehensively studies the radiation performance of canonical antenna elements under the influence of MTHE, aiming at guiding the practical 5G antenna design. It is started by investigating the impacts of chassis, glass and casing, and user's hands on the radiation performance at 28 GHz by using a 5G mobile terminal mock-up. Good agreement is observed between simulation and measurement. For mobile terminals using multi-subarray configurations, we generalize the notion of the coverage efficiency [7] and propose the effective beam-scanning efficiency to represent the coverage performance of a subarray.

The paper is organized as follows. Section II presents the 5G mobile terminal mock-up investigated. Section III presents different kinds of impacts when mmWave antenna elements are integrated in a 5G mobile terminal mock-up. Section IV proposes the effective beam-scanning efficiency to evaluate the impacts on the subarray performance. Section V is the conclusion.

II. 5G MOBILE TERMINAL MOCK-UP INVESTIGATED

A 5G mobile terminal mock-up containing ten antenna elements was modeled as shown in Fig. 1 and fabricated as shown in Fig. 2. The dimensions of the mock-up are 165 mm × 83 mm × 8 mm. The casing is made of PC-ABS ($\epsilon_r = 3.5$) with thickness 1 mm and the display is made of plexiglass ($\epsilon_r = 7.0$) with thickness 0.7 mm. Antennas are printed on a Rogers RO4003 substrate ($\epsilon_r = 3.55$) with thickness 0.3 mm mounted on the chassis. The mock-up contains four kinds of canonical antenna elements operating around 28 GHz, including dipoles (ports 1 and 10), notches (ports 2, 3, 8, and 9), slots (ports 4 and 7), and patches (ports 5 and 6).All of the elements are fed through 50 Ω microstrip lines connected with 50 Ω MMPX-PCB connectors [32].

Air gaps between the antennas and the display and air gaps between the antennas and the casing, as shown in Fig. 1(c), are used to reduce guided waves and impedance mismatch [33]. Additional non-radiating notches cut on the chassis, as shown in Fig. 1, can effectively suppress the guided waves and surface currents flowing in the *y*-direction [7].
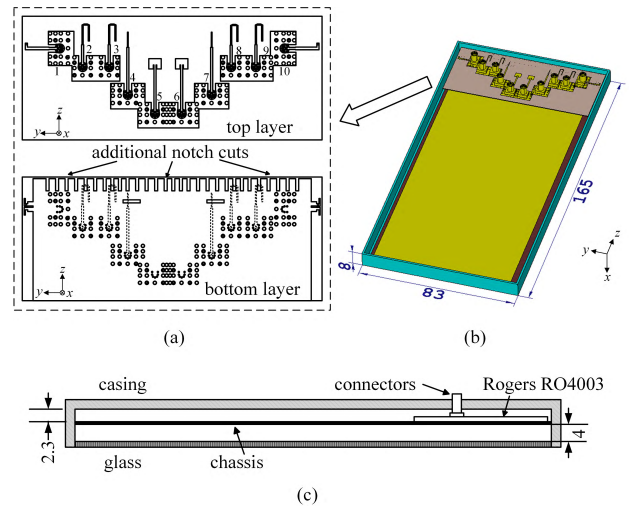

FIGURE 1. Antenna configurations and simulation model. (a) close-up view of antenna configuration, top layer and bottom layer. (b) simulation model with the back cover removed. (c) side view.
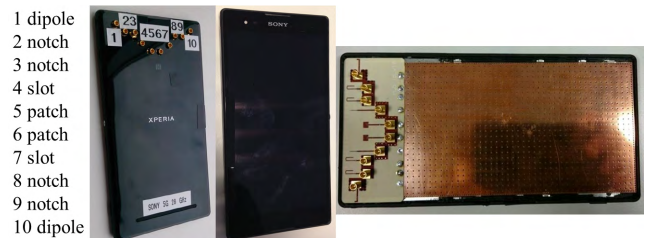

FIGURE 2. Fabricated mock-up: back view, front view, and back view with the back cover removed.

Dipoles (e.g., [20], [25]–[27]), notches (e.g., [7], [15]–[21]), slots (e.g., [12], [15]–[17], [34]), patches (e.g., [7]–[9], [13], [19], [24], [28]), and their evolved forms, such as cavity-backed slot antennas [11], magnetoelectric antennas [29], Yagi-Uda antennas [30], and tightly coupled dipole arrays [31], are the most common types of antenna elements found in the literature about 5G mobile antennas. Moreover, as the dimensions of mobile terminals become much larger than a wavelength, the mobile antenna designers have enough space to implement canonical antenna elements instead of complicated antenna designs like present 2G–4G mobile antennas [35]. Therefore, it is meaningful to investigate radiation performance of canonical antenna elements when integrated in MTHE.

The simplified simulation model is not identical to the fabricated mock-up. Except for the glass, we did not consider other components of the display, such as liquid crystals and the control panel. Rounded corners, screws, feeding cables, and other internal support structures are also not included in the simulation model. For simplicity, only ports 1, 2, 4, and 5 are studied in the following. Antenna elements are fed individually in order to observe their performance. The reflection coefficients of the investigated elements are provided in Appendix A.
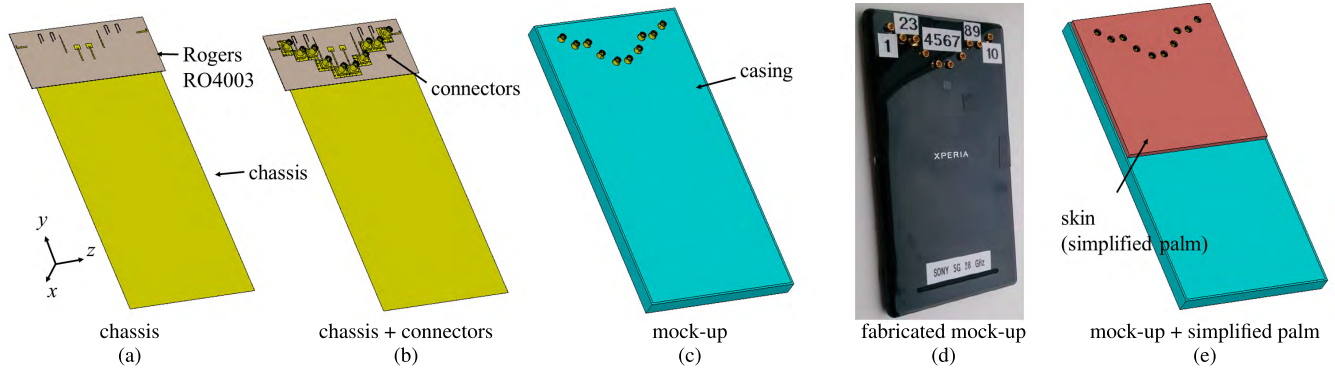
FIGURE 3. Different house integration models for analysis. (The corresponding radiation patterns are shown in Fig. 4 in the same order.) (a) antennas with chassis. (b) antennas with chassis and connectors. (c) complete mock-up. (d) fabricated mock-up. (e) mock-up with the casing half covered by a simplified palm model using a 2 mm-thick skin layer.

III. PERFORMANCE OF VARIOUS ANTENNA ELEMENTS

Mobile terminals can be analyzed as multilayer structures, in which the display and the casing are the superstrates of the printed antennas that may affect the basic antenna performance characteristics [36], [37]. Some mmWave antennas employing multilayer printed circuit boards (PCBs) have more layers of superstrates. A superstrate in the spectral domain can be represented by a portion of equivalent transmission lines, and the far-field strength can be seen as the voltage applied on the loading. Altering the equivalent electrical length and characteristic impedance of the superstrate leads to changes in the radiation patterns [38], [39]. The effects of superstrates may prove either beneficial or detrimental to the antenna performance depending on the specific antenna design, superstrate properties, and performance requirements. In some literature, the effects of superstrates include the effects of guided waves discussed below, but in this paper, the effects of superstrates and the effects of guided waves are distinguished.

Guided waves in dielectric slabs and surface-coated conductors, also called guided-wave modes or surface wave modes [38], [40], [41]. (Literally, surface waves are the waves flowing along the surface of a medium. In some literature, the term 'surface wave' refers to the Zenneck wave existing at the interface between two mediums. One medium has positive permittivity, and the other has negative permittivity, such as in [42]. In some other literature, especially regarding the mmWave frequencies, 'surface wave' refers to the guided waves trapped in dielectric layers, such as in [41].) For practical implementation, the truncation of dielectric slabs leads to guided waves radiating at the edges. Guided waves in dielectric slabs and surface-coated conductors can theoretically exist at all frequencies because there is no cutoff frequency for the TM_0 mode [41]. For the current cellular frequencies, the thickness of dielectric layers (e.g., casing, PCB, display, etc.) is electrically thin, therefore, guided waves are generally not important. In the mmWave frequencies, PCB, displays, and casing become electrically thick such that more modes of guided waves can exist, and the coupling to lower order modes can become stronger [40], [41].

Another phenomena that can be observed affecting radiation performance is surface currents flowing on the chassis. In the current cellular bands below 6 GHz, dimensions of mobile terminals are comparable to the wavelength, and the radiation is produced by the standing-wave modes of surface currents. Such standing-wave modes of surface currents in 2G–4G mobile terminals are sometimes called ground-plane modes [43], chassis modes [44], [45], or characteristic modes [46]–[49]. In the mmWave frequencies, surface currents become propagating waves along the chassis [12], [34] rather than standing waves due to the decreasing wavelength. Guided waves and surface currents have similar behaviors that both can propagate on mobile terminals and radiate at edges, but they originate from different principles.

A. SURFACE CURRENTS ON CHASSIS

First, we examined the effects of surface currents in the absence of the casing, glass, and connectors, as shown in Fig. 3(a). Fig. 4(a) shows the corresponding radiation patterns, and Fig. 5(a) shows the surface currents excited by each antenna element. The strong side lobe of the dipole in $\theta = 180°$ in Fig. 4(a) results from the surface currents along the long edge in Fig. 5(a). Thanks to the additional cutting notch blocking the surface currents, the notch shows the least-disturbed radiation pattern. The slot pattern is bi-directional but has a strong side lobe level due to the surface current excitation. The patch pattern is uni-directional having side lobes at about $\theta = 45°$ and $\theta = 150°$. Both surface currents and guided waves exist for the part with the substrate, i.e. the close-up view in Fig. 1(a). While on the chassis, only surface currents are present when there is no superstrate covering it. According to [12], the main lobe of the slot element excited by the surface currents can appear in the $+z$-direction, in the $-z$-direction, or coincide with the main lobe, depending on the interference of the reflected surface currents from the edges of the chassis, while the superposition condition could be decided by the location of the slot element, the size of the chassis, and the operating frequency.
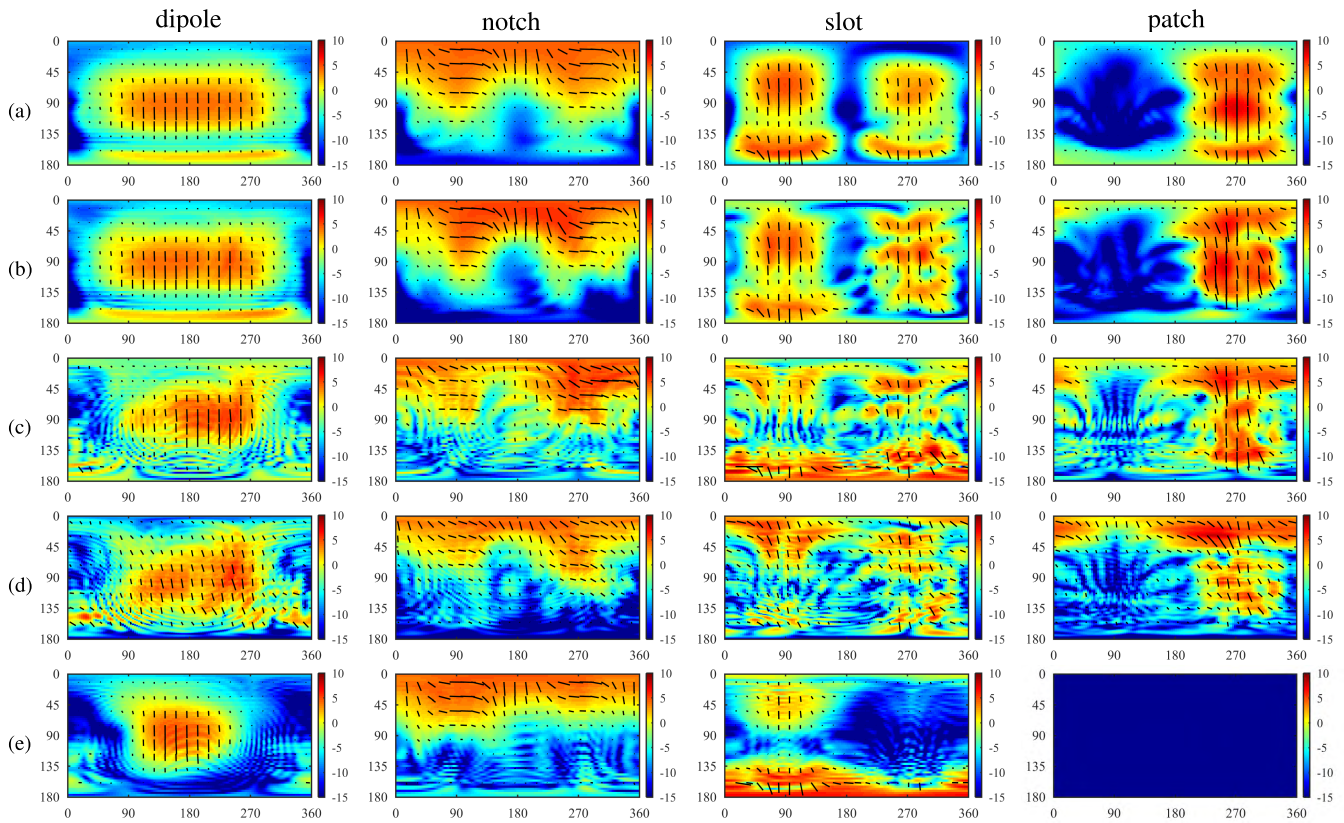
FIGURE 4. Radiation patterns of dipole, notch, slot and patch elements (from left to right). The horizontal axis is the azimuthal angle ϕ in degree, and the vertical axis is the zenith angle θ in degree. The color bar shows the antenna gain ranging from −15 dB to 10 dB. (a)–(e) correspond to Fig. 3(a)–(e) in the same order. (a) antennas with chassis (b) antennas with chassis and connectors (c) complete mock-up (d) measured patterns of fabricated mock-up (e) complete mock-up with simplified palm model. The short black lines indicate the dominant orientation of polarization.

Next, the connectors are added into the model, as shown in Fig. 3(b). At 28 GHz, the connectors are electrically large metallic objects and can be considered as scatterers. In mobile terminals, accessories such as cameras, speakers, microphones, finger scanners, batteries, RF shielding, etc. can also be considered as scatterers. Fig. 4(b) shows the corresponding radiation patterns, and Fig. 5(b) shows that the connectors scatter surface currents (and free space waves). The dipole pattern is least influenced by the scattering, because the dominating surface currents flowing along the chassis are not scattered. A pattern enhancement can be observed for the notch as the surface currents are reflected back to the $+z$-direction by the connectors. Pattern distortion can be observed for the slot and the patch, because the connectors stand into unwanted directions. As a comparison, the pattern in the $+x$-direction, i.e., $\phi \in (0°, 180°)$, is much less distorted than the pattern on the connector side in the $-x$-direction, i.e., $\phi \in (180°, 360°)$. Ultimately, we can state that, scatterers obstructing the excited surface currents greatly influence the radiation patterns, either beneficially, as for the notch, or detrimentally, as for the slot and the patch. Therefore, suppressing unwanted surface currents can effectively improve the pattern performance [34] when the antennas are put in a real mobile terminal in which there are many

scatterers. Of course, design for suppressing surface current and guided waves, such as electromagnetic bandgap (EBG) structures [42] and air cavities [50], can be used, but this is beyond the scope of this paper.

B. IMPACTS OF CASING AND GLASS

In this subsection, the casing and the glass are introduced into the model, as shown in Fig. 3(c). The corresponding radiation patterns are shown in Fig. 4(c). The chassis, casing, glass, and the air gaps form a multilayer structure. The surface currents on the chassis are widely spread out under the influence of the superstrates, as shown in Fig. 5(c). Some similarities can be observed between Fig. 5(b) and Fig. 5(c), such as stronger surface currents on the left side for the dipole, and on the top side for the notch. Fig. 6(a) and (b) show snapshots of the magnitude of electric fields excited by the dipole and the patch, respectively. For the dipole, the plane cut of the fields is chosen excluding the chassis and the connectors, as shown in Fig. 6(a). Stronger guided waves can be observed in the casing than in the glass, because the air gap between the casing and the chassis is smaller than the air gap between the glass and the antenna, thus more power is coupled into the casing. For the patch, the plane cut of the fields is chosen containing the connector and the chassis, as shown in Fig. 6(b).
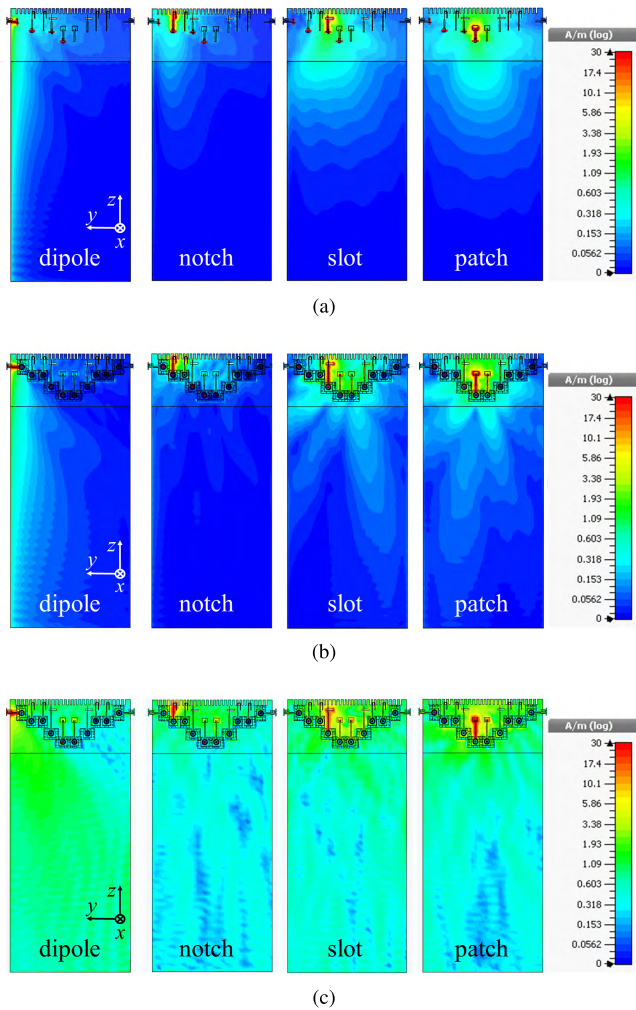
(a)

(b)

(c)

FIGURE 5. Surface currents on chassis (a) antennas with chassis (b) antennas with chassis and connectors. (c) complete mock-up.

The chassis splits the space into two parts, one with the patch and the casing, the other with the glass. Guided waves can also be observed in the casing, but are much weaker than those in Fig. 6(a) due to the scattering of the connector. The fields produced by the patch in the casing side are bounced back from the top bezel (+z-direction) and then propagate in the glass side. Space waves dominate between the glass and the chassis, while very weak guided waves are observed trapped in the glass. The effects of superstrates contribute to more distorted patterns with a large amount of ripples, as shown in Fig. 4(c). The radiation efficiencies of different elements investigated are shown in Table 1. The presence of casing and glass reduces the radiation efficiency by 8.3%, 5.8%, 5.2%, and 4.6% for dipole, notch, slot, and patch, respectively.

Fig. 4(d) shows the radiation patterns measured using Microwave Vision Group (MVG) StarLab 5G near-field (NF) system [51]. The measured patterns in Fig. 4(d) agree well with the simulated patterns in Fig. 4(c) except for the slot pattern. The measured slot pattern radiates more in the
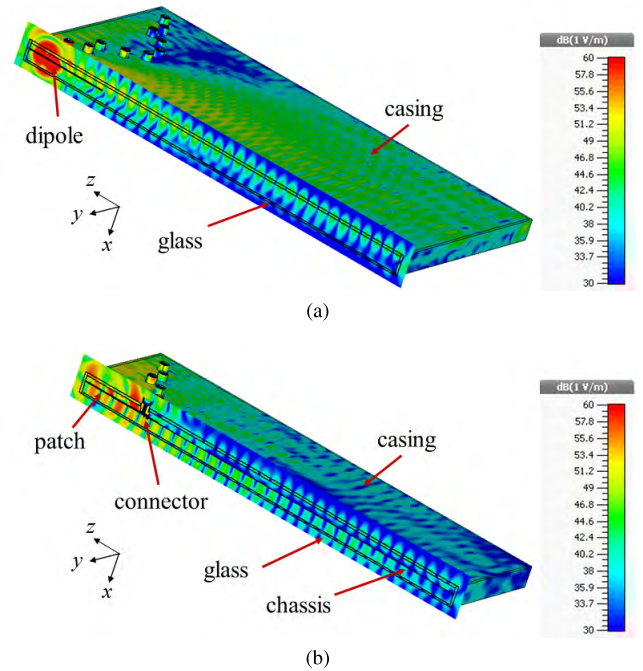

(a)

(b)

FIGURE 6. Snapshots of the magnitude of the electric-field distributions (a) dipole (b) patch.

TABLE 1. Radiation efficiency with and without glass and casing.

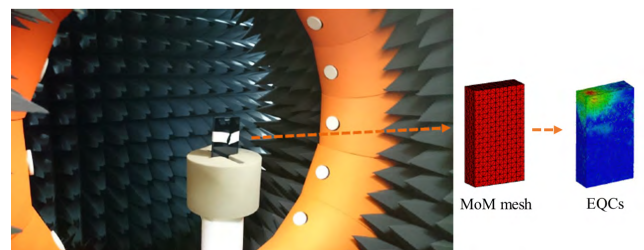|	w/o glass and casing	with glass and casing
dipole	95.4%	87.1%
notch	93.2%	87.4%
slot	92.2%	87.0%
patch	85.4%	80.8%

FIGURE 7. Antenna measurement and diagnosis using MVG StarLab 5G NF system [51] and INSIGHT [52].

+z-direction while the simulated pattern radiates more towards the −z-direction. This may be attributed to the property that the pattern of the slot is determined by superposition of surface currents and/or guided waves reflected from the edges as mentioned before [12]. Due to the fact that our simulation model is not identical to the fabricated mock-up, such a sensitive superposition condition could be changed and lead the pattern to radiate in other directions.

Realistic channel environments can introduce large fluctuations of the received signal strength when the mobile
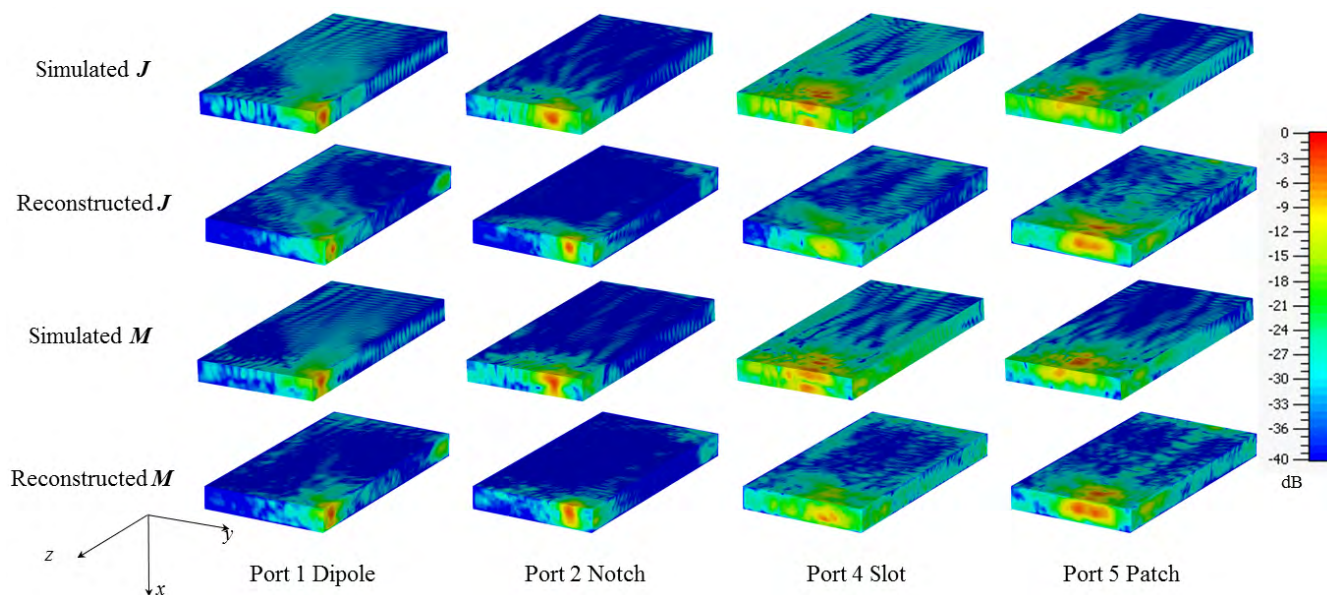
FIGURE 8. Simulated and reconstructed EQCs.

terminal's orientation is arbitrary, even in the line-of-sight (LOS) radio links. Therefore, multi-input multi-output (MIMO) antennas transmitting orthogonally-polarized signals are recommended to increase the channel capacity and reduce the outage possibility [15], [17], [53], [54]. The dominant polarization of each model and each element is presented by the short black lines in Fig. 4. The simulation and measurement results show that MTHE has limited effects on polarization, except for the slot element. Due to the severely-distorted patterns, it is hard to compare the polarization performance of the slot element in Fig. 3(c), (d), and (e).

In 5G mobile terminals, the footprint of an entire mmWave antenna array could be much smaller than the footprint of a single antenna in the 2G–4G mobile terminals because of the shorter wavelength. Due to the decreasing footprint of antennas and beam-forming implementation, co-design of antennas and RF front ends, or antenna in package (AiP) are of importance in achieving high-throughput communication [54], [55]. However, the co-design of antennas and terminal housing is challenging even for today's mobile terminals. As long as the antennas are located inside the casing, the impact of superstrates and guided waves may be significant in mmWave bands and can hardly be eliminated. The casing and the display not only change the radiation patterns, but also cause impedance mismatch, if the antenna is very close to the superstrates. Although one can tune the geometric parameters of antenna elements to reach the impedance matching condition, such pattern distortion independent of the matched impedance would still exist. To mitigate the terminal housing effects brought by the casing and glass, low-permittivity materials are preferable, and antennas should be placed slightly away from them [33], [41].

C. EXPERIMENTAL VALIDATION: NEAR-FIELD ANTENNA DIAGNOSIS

Previously, the impacts on the antenna performance caused by the components in mobile terminals can be observed through the distorted far-field (FF) patterns. An alternative way to visualize the effects is using the inverse source technique [56]–[63] to obtain equivalent currents (EQCs) on a given 3D closed surface surrounding the mobile terminal. The inverse source technique implemented in the MVG software INSIGHT [52] and reported in [58] allows the extreme near field and currents to be reconstructed on an arbitrary 3D surface from measured NF or FF data.

MVG StarLab 5G is a newly designed portable spherical multi-probe system where an array of probes is used to electronically scan the radiated field intended for NF measurements in the 6 to 50 GHz frequency range [51]. The fields were measured using StarLab 5G, as shown in Fig. 7, and the measured data used for the FF pattern through NF-to-FF transformation in the previous section was reused for EQC reconstruction by using INSIGHT. The size of the closed reconstructed surface, 171 mm × 89 mm × 14 mm, is chosen slightly larger than the mobile terminal surface to reduce the positioning error. The simulated EQCs on the reconstructed surface can be obtained in CST by directly applying Love's equivalence theorem, while the simulated EQCs contain those from non-radiated fields. Fig. 8 present the reconstructed and simulated EQC results. Generally, the reconstructed EQCs agree well with the simulated. The slot and the patch have wider EQC distribution while the dipole and the notch have more constrained EQC distribution. This agrees with that the slot and the patch have more severe pattern distortion in Fig. 4(c) and Fig. 4(d). For the dipole and the notch, a portion of reconstructed EQCs can be observed in the corner

stronger than the simulated EQCs in the same location. This may be attributed to the fabrication discrepancy and cable effects.

When implementing antennas into the mobile terminals in practice, the precise and complete information of mechanical and electronic characteristics needed for full-wave simulation is unavailable, particularly critical in mmWave frequencies where the surrounding components have remarkable effects on the radiation performance. Although measurements of radiation patterns are widely required for validation, FF patterns may not provide enough information for adjustment. To authors' best knowledge, it is the first time applying the inverse source technique on 5G mobile terminals. Such technique provides intuitive physical insight and extra diagnostic information about 5G mobile antenna design. The reconstructed EQCs can facilitate further adjustment from a brand new perspective.

D. EFFECTS OF USER's HAND

Effects of the user's hand are critical issues for mobile terminals. The energy penetration depth of tissue is less than 2 mm at 15 GHz and less than 1 mm at 30 GHz [64]. The skin on the palm is the thickest part on the human body, and can be as thick as 2 mm. In our study, a homogeneous medium with skin material is set with relative permittivity of 16.6 and conductivity of 25.8 S/m at 28 GHz [65]. At 28 GHz, the user's hand is an electrically large object, and the full-wave simulation is very time-consuming. To facilitate the simulation, simplified models are introduced to investigate the effects of the user's hand, as shown in Fig. 3(d) and Fig. 9.
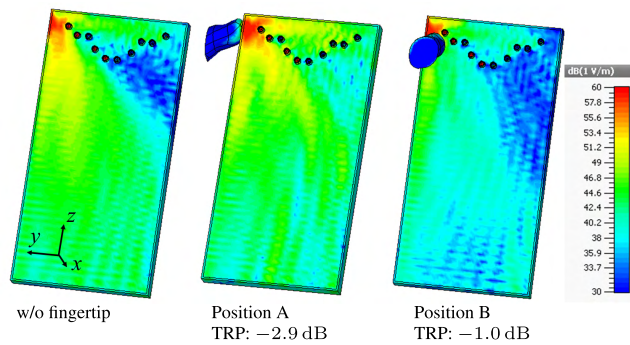

FIGURE 9. Electric field distributions when a fingertip touches the casing. Compared to the TRP without the finger tip, the TRP of Position A and Position B drops 2.9 dB and 1.0 dB, respectively.

1) PALM

A layer of skin with thickness of 2 mm is used to simulate the palm covering the casing because using a full-hand model is very time-consuming. The simulated patterns are shown in Fig. 4(e). The covering skin in the $-x$-direction corresponds to the solid angle $\phi \in (180°, 360°)$. Compared to Fig. 4(c), the patterns of the dipole, the notch, and the slot are squeezed out of these solid angles due to the high permittivity and loss of the skin. The skin layer completely

blocks the radiation from the patch and almost all the power is lost in the skin layer, thus the patch suffers from very low radiation efficiency and its gain is lower than -15 dB. The total radiated power (TRP) drops 1.6 dB, 1.2 dB, 2.6 dB, and 22.3 dB for the dipole, the notch, the slot, and the patch, respectively.

2) FINGERTIP

A piece of a fingertip is added into the model to study the impact on the antenna performance, exemplified by the dipole element. Two scenarios are studied, as shown in Fig. 9. The fingertip touches the casing on the lateral bezel upon the dipole, denoted as 'Position A' and slightly away from the location of the dipole on the casing, denoted as 'Position B'. When the fingertip is placed at Position A, it causes a 2.9 dB drop in the TRP. Stronger guided waves, which may be attributed to the reflection due to the high permittvity of the skin, can also be observed flowing along the casing. The corresponding pattern is shown in Fig. 10(a). Because the fingertip blocks the main radiation direction, the radiation is reflected towards the $+y$-direction, i.e., $\phi = 270°$. When the fingertip is placed at Position B, about 10 mm away from the dipole, the guided waves becomes weaker. It appears as though the fingertip 'assimilates' the guided waves. For multilayer structures, the guided waves are prone to becoming trapped in the electrically thick layers. The electrical thickness of the fingertip is much higher than the casing's, thus can be seen as a small piece of a superstrate upon the casing. A portion of the guided waves is guided into the skin layer and transformed into dielectric loss. The fingertip placed at Position B also reflects parts of the radiation, leading to a radiation pattern squeezed towards the $-y$-direction, i.e., $\theta > 90°$, as shown in Fig. 10(b).
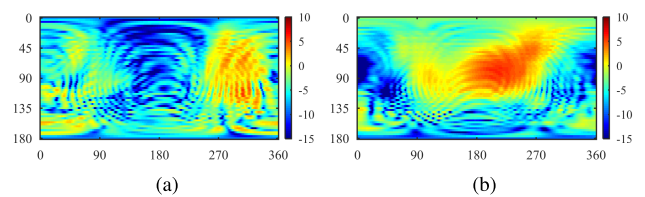

FIGURE 10. Radiation patterns with a fingertip (a) Position A (b) Position B. The horizontal axis is the azimuthal angle ϕ in degree, and the vertical axis is the zenith angle θ in degree, using the coordinate system in Fig. 1. The color bar shows the antenna gain ranging from -15 dB to 10 dB.

The models considered above are two extreme situations for the effects of the user's hand. On one hand, the effects in practice would produce more TRP loss than the fingertip results. On the other hand, the user's hand probably would not cover all of the operating antennas. The simplified palm results and the fingertip results suggest that, as long as the hand or the finger do not entirely cover the antenna, the antenna can still have acceptable performance. When directly touching mobile terminals but not shielding the antennas, the user's hand would twist the guided waves and patterns towards the opposite directions against

the hands and add several dB losses. To mitigate the effects of the user's hand, distributed antenna arrays with switched diversity, in which, if one subarray is unable to transmit, another subarray can transmit alternatively, are the common solution [9], [11].

3) OTHER EFFECTS OF USER's BODY

There are various published user's body effect studies[1] for 5G mmWave user equipment [12], [16]–[18]. The major effects of the user's body in mmWave frequencies are radiated power absorption and body blocking effects, when a person holds a mobile terminal but does not directly block the antenna. The radiated power absorption is lower compared to the frequency bands below 6 GHz. At 15 GHz and 28 GHz, the drop in TRP is only about 2 dB in the data mode and 3–4 dB in the talking mode [17], much lower than their counterparts in the current cellular bands (e.g., typically 6–10 dB in the talking mode) [35]. The body blocking effects become much more severe in the mmWave bands and a human shadow can be clearly observed in the 2D pattern [16]–[18]. A typical estimate of the body blocking loss in the link budget is 30 dB [66].

IV. PERFORMANCE EVALUATION OF ARRAY CONFIGURATIONS

In the previous section, the performance of different antenna elements was studied. For the forthcoming 5G mmWave user equipment, array antennas would be deployed to provide not only extra array gain but also beam-scanning capability [7], [67], as mmWave communications suffer from higher path loss than current cellular communications. Thus, array performance in MTHE is of particular interest for 5G antenna design. The coverage performance of array configurations, in terms of coverage efficiency, was studied in [7], [8], [12], and [16], but how MTHE affects the coverage performance lacks investigation. More importantly, the coverage efficiency is unable to represent the coverage performance of a subarray, as revealed in this section. Instead, the effective beam-scanning efficiency is proposed to quantify it, and based on the effective beam-scanning efficiency, the coverage performance of subarrays in MTHE and how it influences the entire coverage performance of the multi-subarray configuration are studied.

A. COVERAGE EFFICIENCY AND ARRAY CONFIGURATION

In the earlier work [7], to evaluate the beam-scanning capability of array antennas in mobile terminals, the coverage efficiency, η_c, was proposed

$$\eta_c = \frac{\text{Coverage Solid Angle}}{\text{Total Solid Angle}} = \frac{\Omega_c}{\Omega_0}, \quad (1)$$

in which

$$\Omega_c = \int_{\Omega_0} h\left(G_{TS}\left(\Omega\right)\right) d\Omega. \quad (2)$$

and h is a step function

$$h\left(G_{TS}\right) = \begin{cases} 1 & G_{TS} \geq G_{min} \\ 0 & G_{TS} < G_{min}, \end{cases} \quad (3)$$

Ω_c is the coverage solid angle for which the total scan pattern, G_{TS}, is higher than the minimum required gain, G_{min}, satisfying the system requirements; Ω_0 is the full-spherical coverage solid angle, i.e., 4π steradians.

To realize full-spherical coverage, a few subarrays are preferable, as has been proposed in 3GPP [68]. Fig. 11 shows the possible coverage using a single array or a set of subarrays. References [7] and [68] proposed to use a single array with an 8×1 liner array or two 4×1 or 2×2 subarrays. These kinds of array configuration may result in blind angles due to limitations of the element patterns or gain reduction in the end-fire directions. In order to realize full-spherical coverage, [8] and [12] proposed to use three subarrays such that the patterns of the additional subarrays overlap with the patterns of other subarrays. 5G mobile terminals could possibly utilize more subarrays, e.g., Fig. 11(b), in which each subarray deploying more directive antenna elements could have more constrained coverage and thus higher gain.
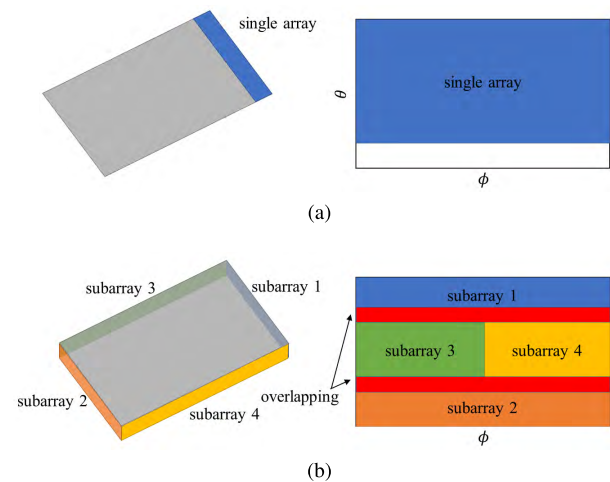

FIGURE 11. Possible array configurations (*left*) and coverage (*right*) for 5G mmWave mobile terminals (a) single array [7] (b) four subarrays.

Based on the above discussion, the η_c of different array configurations are examined. Fig. 12 shows the schematic array configurations using the notch element and the dipole element analyzed in the previous sections as they have better radiation patterns than the slot and the patch. The element patterns in Fig. 4 are treated as the embedded patterns in the array, as in [16]. To enable beam scanning, the progressive phase shift scheme is adopted as in [19] with phase shift difference changing from $-150°$ to $150°$ for every $75°$ and with element spacing of half a wavelength. The total scan patterns
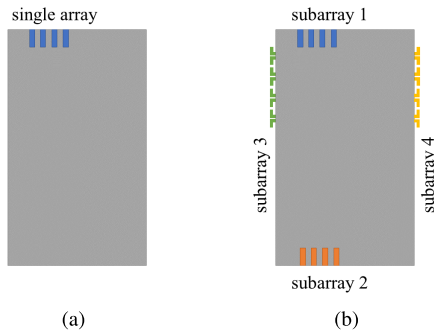
FIGURE 12. Illustration of array configurations referring to Fig. 11. (a) 4 × 1 single notch array, (b) four subarray configuration with two 4 × 1 notch subarrays and two 4 × 1 dipole subarrays.

of the 4 × 1 dipole and 4 × 1 notch arrays/subarrays are shown in Fig. 13. The choices of the element spacing and the phase excitations ensure that no grating lobe is generated while also ensuring that each subarray has sufficiently wide coverage. The resulting η_c is shown in Fig. 14. Adding the casing and glass lead to a drop of the η_c for the four-subarray configuration due to the undesirable coverage of each subarray.
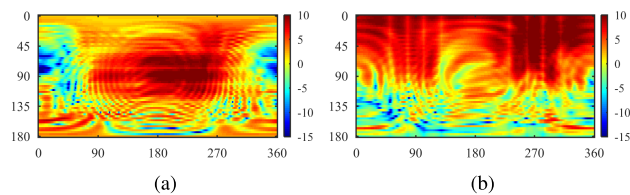

FIGURE 13. Total scan patterns using measured element patterns. (a) 4 × 1 dipole array. (b) 4 × 1 notch array. The horizontal axis is the azimuthal angle ϕ in degree, and the vertical axis is the zenith angle θ in degree, using the coordinate system in Fig. 1. The color bar shows the antenna gain ranging from −15 dB to 10 dB.
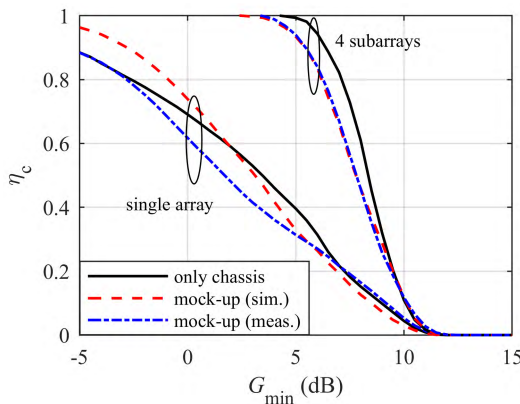

FIGURE 14. The coverage efficiency of different array configurations.

For the single array that is reused as the subarray in Fig. 12(b), however, it is not evident that the casing and glass are detrimental to η_c. As suggested in Fig. 15, the terminal housing effects direct the coverage of a subarray to the undesired solid angles. The coverage distortion could be small (see Fig. 15(a)), or could be severe (see Fig. 15(b)). However, η_c is integrated over the entire sphere, as suggested

in (1)–(3), Fig. 15(a) and (b) can lead to the same levels of η_c. Therefore, the undesirable radiation cannot be appropriately revealed by η_c for a subarray.
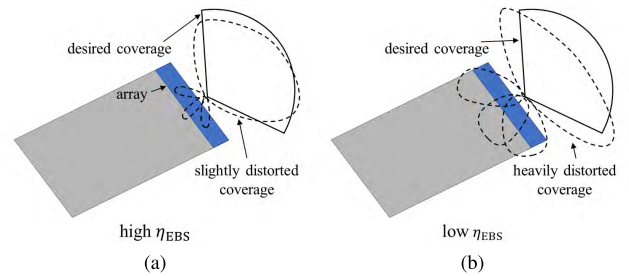

FIGURE 15. Illustration of effective beam-scanning efficiency. (a) If a beam-scanning subarray is less affected by MTHE and has less distorted coverage, it results in a high effective beam-scanning efficiency. (b) If a beam-scanning subarray is more affected by MTHE and has more distorted coverage, it results in a low effective beam-scanning efficiency.

B. EFFECTIVE BEAM-SCANNING EFFICIENCY

As η_c is not suitable for subarrays, we propose the effective beam-scanning efficiency (EBS) to evaluate the beam-scanning performance of a subarray. Assuming that the number of beams is N for the subarray, the effective beam-scanning efficiency is

$$\eta_{\text{EBS}}\left(G_{\min}, \Omega_{\text{d}}\right) = \frac{\int_{\Omega_{\text{d}}} |F_{\text{TS}}(\Omega)|^2 \, h\left(G_{\text{TS}}(\Omega)\right) \, d\Omega}{\int_{\Omega_0} |F_{\text{TS}}(\Omega)|^2 \, d\Omega}, \quad (4)$$

in which $|F_{\text{TS}}(\Omega)|$ denotes the far-field strength for the total scan pattern

$$|F_{\text{TS}}(\Omega)| = \max_{i=1,2,\dots,N} |F_i(\Omega)|, \quad (5)$$

where $|F_i| = \sqrt{|F_{i,\theta}|^2 + |F_{i,\phi}|^2}$ is the far-field strength of each scan beam.

If a beam-scanning subarray is less affected by MTHE and has less distorted coverage, it leads to a high η_{EBS}, as shown in Fig. 15(a). In contrast, the severely-distorted coverage gives a low η_{EBS}, as shown in Fig. 15(b). If all the energy is radiated within Ω_{d} satisfying the minimum required gain $G_{\min}$, η_{EBS} should be equal to 1. As no such array can focus all the energy within certain Ω_{d}, η_{EBS} is always below 1. When the radiation pattern is distorted, η_{EBS} drops as some energy is radiated in other directions. The desired solid angle Ω_{d} should be chosen considering the element pattern and entire array coverage, such as those in Fig. 11. Desired coverage solid angles of different subarrays comprise the full-spherical coverage, i.e., $\Omega_0 = \{\Omega_{\text{d1}} \cup \Omega_{\text{d2}} \cup, \dots, \cup \Omega_{\text{d}M}\}$, where M is the number of subarrays. The way to choose Ω_{d} is not unique, and in this paper, the way we choose Ω_{d} for the dipole array and the notch array is provided in Appendix B. Note that η_{EBS} is inherently consistent with η_c, i.e., $\eta_{\text{EBS}}(\Omega_{\text{d}} = \Omega_0) = \eta_c$. Denote the fraction of energy of the total scan pattern flowing across Ω_{d} as

$$\eta_{\text{EBS0}} = \eta_{\text{EBS}}(G_{\min} = -\infty, \Omega_{\text{d}}), \quad (6)$$

TABLE 2. Minimum Ω_d satisfying $\eta_{EBS0} = 0.8$ and $\eta_{EBS0} = 0.6$.

	η_{EBS0}	Ω_d
dipole subarray	0.8	$\theta \in [48°, 132°], \phi \in [44°, 316°]$
	0.6	$\theta \in [57°, 123°], \phi \in [79°, 281°]$
notch subarray	0.8	$\theta \in [0°, 90°], \phi \in [0°, 360°]$
	0.6	$\theta \in [0°, 68°], \phi \in [0°, 360°]$

in which G_{min} is in dB. Using Ω_d listed in Table 2, Appendix B, the corresponding η_{EBS} is shown in Fig. 16. For each subarray and different η_{EBS0} levels, $\eta_{EBS0} = 0.8$ and $\eta_{EBS0} = 0.6$ give similar η_{EBS} behaviors. The connectors have a negligible effect on the scattering for the dipole and does not significantly change its η_{EBS}. The connectors enhancing the embedded element pattern of the notch, as shown in Fig. 4(b), lead to a slight increase of η_{EBS} for the notch subarray. The effects of superstrates and guided waves result in a detrimental η_{EBS} for both subarrays. Although the total energy flow across Ω_d is almost the same with and without the casing and glass, a higher η_{EBS} for large G_{min} and a lower η_{EBS} for small G_{min} suggest that the existence of the casing and glass squeezes the patterns to a limited solid
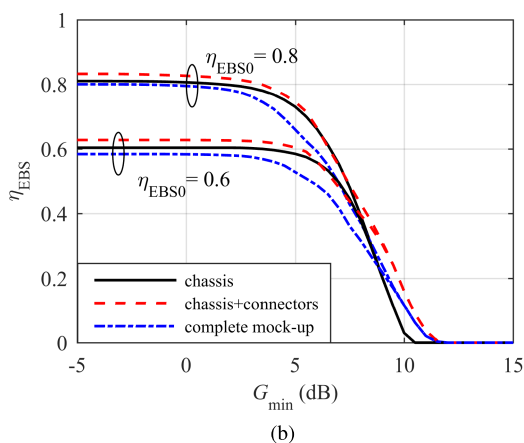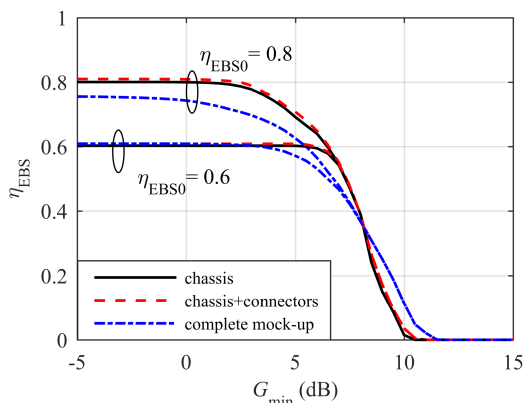
angle and finally result in a drop of η_c for the multi-subarray configuration in Fig. 14.

In practice, there are few choices of casing material and its thickness. Nevertheless, lower permittivity and thinner material is preferable for the casing of mobile terminals to achieve better array performance, as the effects of superstrates and guided waves become weak for electrically thin superstrates. Many other factors, such as placement and the size of mobile terminals, make the coverage distortion more complicated. The effective beam-scanning efficiency, η_{EBS}, would be a useful performance indicator for the evaluation of the beam-scanning/coverage performance of subarrays/arrays and could be treated as an optimization goal for 5G antenna design.

V. CONCLUSION

In this paper, various canonical antenna elements are integrated in a 5G mobile terminal mock-up operating at 28 GHz. The radiation performance of the investigated antenna elements suffers from the terminal housing effects. At the first time for 5G mmWave mobile antennas, the effects of superstrates, guided waves, surface currents, and the user's hand on the radiation performance are identified and analyzed separately. The EQCs obtained through the inverse source technique provide a brand new perspective of facilitating 5G mobile antenna design in MHTE. In this work, good agreement of EQCs is obtained between simulation and measurement. The terminal housing effects on array and subarray performance are evaluated via the coverage efficiency and the proposed effective beam-scanning efficiency. Future 5G mobile antenna research needs to take these impacts into consideration. The effective beam-scanning efficiency, together with the coverage efficiency, can be useful performance indicators for 5G beam-scanning mobile terminals.

APPENDIX A
REFLECTION COEFFICIENTS OF ANTENNA ELEMENTS IN FABRICATED MOCK-UP
Fig. 17 shows the measured reflection coefficients of the fabricated mock-up. All the investigated elements resonate
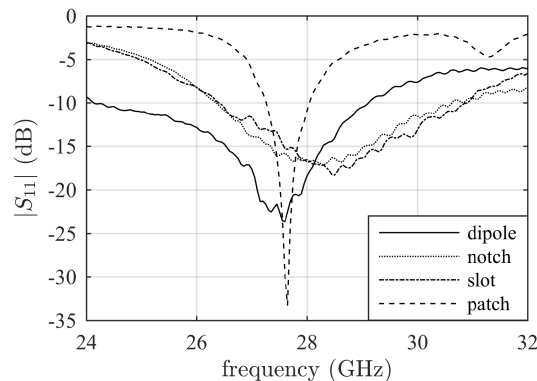
FIGURE 16. The effective beam-scanning efficiency (a) 4 × 1 dipole array (b) 4 × 1 notch array.

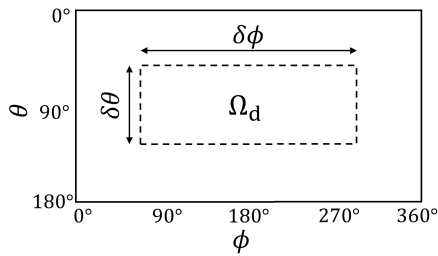**FIGURE 17.** Measured $|S_{11}|$ of fabricated mock-up.

FIGURE 18. Illustration of the choice of Ω_d.

around 28 GHz. The bandwidth of the patch element is relatively narrow compared with other elements due to the thin substrate. By increasing the substrate thickness or taking other measures, the patch antenna can achieve enough wide bandwidth for 5G mmWave communication [69]. Nevertheless, this paper focuses on the general effects of MTHE on the radiation performance of canonical antennas rather than the operating bandwidth of specific antenna design.

APPENDIX B
CHOOSE DESIRED SOLID ANGLES FOR DIPOLE ARRAY AND NOTCH ARRAY

In this paper, Ω_d, as shown in Fig. 18, is defined as

$$\Omega_d = \delta\theta \times \delta\phi, \qquad (7)$$

where $\delta\theta$ and $\delta\phi$ are the zenith and azimuthal angles of Ω_d, respectively.

Table 2 shows the minimum Ω_d satisfying $\eta_{EBS0} = 0.8$ and $\eta_{EBS0} = 0.6$ for the dipole and notch subarrays in the absence of the connectors, the casing, and glass.

ACKNOWLEDGEMENT

The authors thank Mr. Wang He at the Centre for Optical and Electromagnetic Research, Zhejiang University for his help with literature review.

REFERENCES

[1] *IMT Vision'S Framework and Overall Objectives of the Future Development of IMT for 2020 and Beyond*, document Rec. ITU-R M.2083-0, ITU-R, Sep. 2015, pp. 1–19.

[2] *Technical Feasibility of IMT in Bands Above 6 GHz*, document ITU-R M.2376-0, ITU-R, Jul. 2015, pp. 1–132.

[3] *Final Acts WRC-15*, ITU-R, World Radiocommunication Conference. 2015.

[4] *Further Notice of Proposed Rulemaking*, FCC, Washington, DC, USA, Jul. 2016.

[5] "Opinion on spectrum related aspects for next-generation wireless systems (5G)," Radio Spectr. Policy Group, Brussels, Belgium, Tech. Rep. RSPG16-032, Nov. 2016, pp. 1–6.

[6] "5G radio access," Ericsson, Stockholm, Sweden, White Paper Uen 284 23-3204 Rev C, Apr. 2016. [Online]. Available: https://www.ericsson.com/assets/local/publications/white-papers/wp-5g.pdf

[7] J. Helander, K. Zhao, Z. Ying, and D. Sjöberg, "Performance analysis of millimeter-wave phased array antennas in cellular handsets," *IEEE Antennas Wireless Propag. Lett.*, vol. 15, pp. 504–507, 2016.

[8] N. Ojaroudiparchin, M. Shen, S. Zhang, and G. F. Pedersen, "A switchable 3-D-coverage-phased array antenna package for 5G mobile terminals," *IEEE Antennas Wireless Propag. Lett.*, vol. 15, pp. 1747–1750, Feb. 2016.

[9] Y. Huo, X. Dong, and W. Xu, "5G cellular user equipment: From theory to practical hardware design," *IEEE Access*, vol. 5, pp. 13992–14010, 2017.

[10] W. Hong, K.-H. Baek, and S. Ko, "Millimeter-wave 5G antennas for smartphones: Overview and experimental demonstration," *IEEE Trans. Antennas Propag.*, vol. 65, no. 12, pp. 6250–6261, Dec. 2017.

[11] B. Yu, K. Yang, C.-Y.-D. Sim, and G. Yang, "A novel 28 GHz beam steering array for 5G mobile device with metallic casing application," *IEEE Trans. Antennas Propag.*, vol. 66, no. 1, pp. 462–466, Jan. 2018.

[12] S. Zhang, X. Chen, I. Syrytsin, and G. F. Pedersen, "A planar switchable 3-D-coverage phased array antenna and its user effects for 28-GHz mobile terminal applications," *IEEE Trans. Antennas Propag.*, vol. 65, no. 12, pp. 6413–6421, Dec. 2017.

[13] J. Hejselbæk, J. Ø. Nielsen, W. Fan, and G. F. Pedersen, "Measured 21.5 GHz indoor channels with user-held handset antenna array," *IEEE Trans. Antennas Propag.*, vol. 65, no. 12, pp. 6574–6583, Dec. 2017.

[14] I. Syrytsin, S. Zhang, and G. F. Pedersen, "User impact on phased and switch diversity arrays in 5G mobile terminals," *IEEE Access*, vol. 6, pp. 1616–1623, 2018.

[15] Z. Ying *et al.*, "Multiplexing efficiency of high order MIMO in mobile terminal for 5G communication at 15 GHz," in *Proc. Int. Symp. Antennas Propag. (ISAP)*, Oct. 2016, pp. 594–595.

[16] K. Zhao, J. Helander, D. Sjöberg, S. He, T. Bolin, and Z. Ying, "User body effect on phased array in user equipment for the 5G mmWave communication system," *IEEE Antennas Wireless Propag. Lett.*, vol. 16, pp. 864–867, 2017.

[17] K. Zhao *et al.*, "Channel characteristics and user body effects in an outdoor urban scenario at 15 and 28 GHz," *IEEE Trans. Antennas Propag.*, vol. 65, no. 12, pp. 6534–6548, Dec. 2017.

[18] I. Syrytsin, S. Zhang, G. F. Pedersen, K. Zhao, T. Bolin, and Z. Ying, "Statistical investigation of the user effects on mobile terminal antennas for 5G applications," *IEEE Trans. Antennas Propag.*, vol. 65, no. 12, pp. 6596–6605, Dec. 2017.

[19] B. Xu *et al.*, "Power density measurements at 15 GHz for RF EMF compliance assessments of 5G user equipment," *IEEE Trans. Antennas Propag.*, vol. 65, no. 12, pp. 6584–6595, Dec. 2017.

[20] D. Colombi, B. Thors, C. Törnevik, and Q. Balzano, "RF energy absorption by biological tissues in close proximity to millimeter-wave 5G wireless equipment," *IEEE Access*, vol. 6, pp. 4974–4981, 2018.

[21] B. Xu, M. Gustafsson, S. Shi, K. Zhao, Z. Ying, and S. He, "Radio frequency exposure compliance of multiple antennas for cellular equipment based on semidefinite relaxation," *IEEE Trans. Electromagn. Compat.*, to be published.

[22] D. Colombi, B. Thors, and C. Törnevik, "Implications of EMF exposure limits on output power levels for 5G devices above 6 GHz," *IEEE Antennas Wireless Propag. Lett.*, vol. 14, pp. 1247–1249, 2015.

[23] K. Zhao, Z. Ying, and S. He, "EMF exposure study concerning mmWave phased array in mobile devices for 5G communication," *IEEE Antennas Wireless Propag. Lett.*, vol. 15, pp. 1132–1135, 2016.

[24] W. He, B. Xu, M. Gustafsson, Z. Ying, and S. He, "RF compliance study of temperature elevation in human head model around 28 GHz for 5G user equipment application: Simulation analysis," *IEEE Access*, vol. 6, pp. 830–838, 2018.

[25] B. Thors, D. Colombi, Z. Ying, T. Bolin, and C. Törnevik, "Exposure to RF EMF from array antennas in 5G mobile communication equipment," *IEEE Access*, vol. 4, pp. 7469–7478, 2016.

[26] S. Zihir, O. D. Gurbuz, A. Kar-Roy, S. Raman, and G. M. Rebeiz, "60-GHz 64- and 256-elements wafer-scale phased-array transmitters using full-reticle and subreticle stitching techniques," *IEEE Trans. Microw. Theory Techn.*, vol. 64, no. 12, pp. 4701–4719, Dec. 2016.

[27] I. Syrytsin, S. Zhang, G. F. Pedersen, and A. Morris, "Compact quad-mode planar phased array with wideband for 5G mobile terminals," *IEEE Trans. Antennas Propag.*, to be published.

[28] S.-J. Park, D.-H. Shin, and S.-O. Park, "Low side-lobe substrate-integrated-waveguide antenna array using broadband unequal feeding network for millimeter-wave handset device," *IEEE Trans. Antennas Propag.*, vol. 64, no. 3, pp. 923–932, Mar. 2016.

[29] J. Wang, Y. Li, L. Ge, J. Wang, and K.-M. Luk, "A 60 GHz horizontally polarized magnetoelectric dipole antenna array with 2-D multi-beam endfire radiation," *IEEE Trans. Antennas Propag.*, vol. 65, no. 11, pp. 5837–5845, Nov. 2017.

[30] Y.-W. Hsu, T.-C. Huang, H.-S. Lin, and Y.-C. Lin, "Dual-polarized quasi Yagi–Uda antennas with endfire radiation for millimeter-wave MIMO terminals," *IEEE Trans. Antennas Propag.*, vol. 65, no. 12, pp. 6282–6289, Dec. 2017.

[31] Y. Wang, L. Zhu, H. Wang, Y. Luo, and G. Yang, "A compact, scanning tightly coupled dipole array with parasitic strips for next-generation wireless applications," *IEEE Antennas Wireless Propag. Lett.*, vol. 17, no. 4, pp. 534–537, Apr. 2018.

[32] *HUBER+SUHNER*. [Online]. Available: http://www.hubersuhner.com/en/Products/Radio-Frequency/Connectors

[33] K.-L. Wong, Y.-T. Cheng, and J.-S. Row, "Resonance in a superstrate-loaded cylindrical-rectangular microstrip structure," *IEEE Trans. Microw. Theory Techn.*, vol. 41, no. 5, pp. 814–819, May 1993.

[34] B. Xu, K. Zhao, Z. Ying, S. He, and J. Hu, "Investigation of surface waves suppression on 5G handset devices at 15 GHz," in *Proc. 10th Eur. Conf. Antennas Propag. (EuCAP)*, Apr. 2016, pp. 1–4.

[35] Z. Ying, "Antennas in cellular phones for mobile communications," *Proc. IEEE*, vol. 100, no. 7, pp. 2286–2296, Jul. 2012.

[36] N. G. Alexópoulos and D. R. Jackson, "Fundamental superstrate (cover) effects on printed circuit antennas," *IEEE Trans. Antennas Propag.*, vol. 32, no. 8, pp. 807–816, Aug. 1984.

[37] D. Jackson and N. Alexópoulos, "Analysis of planar strip geometries in a substrate-superstrate configuration," *IEEE Trans. Antennas Propag.*, vol. AP-34, no. 12, pp. 1430–1438, Dec. 1986.

[38] N. K. Das and D. M. Pozar, "A generalized spectral-domain Green's function for multilayer dielectric substrates with application to multilayer transmission lines," *IEEE Trans. Microw. Theory Techn.*, vol. MTT-35, no. 3, pp. 326–335, Mar. 1987.

[39] X. H. Wu, A. A. Kishk, and A. W. Glisson, "A transmission line method to compute the far-field radiation of arbitrarily directed hertzian dipoles in a multilayer dielectric structure: Theory and applications," *IEEE Trans. Antennas Propag.*, vol. 54, no. 10, pp. 2731–2741, Oct. 2006.

[40] R. F. Harrington, *Time-Harmonic Electromagnetic Fields*. Piscataway, NJ, USA: IEEE Press, 2001.

[41] D. M. Pozar, "Considerations for millimeter wave printed antennas," *IEEE Trans. Antennas Propag.*, vol. AP-31, no. 5, pp. 740–747, Sep. 1983.

[42] D. Sievenpiper, L. Zhang, R. F. J. Broas, N. G. Alexopoulous, and E. Yablonovitch, "High-impedance electromagnetic surfaces with a forbidden frequency band," *IEEE Trans. Microw. Theory Techn.*, vol. 47, no. 11, pp. 2059–2074, Nov. 1999.

[43] A. Cabedo, J. Anguera, C. Picher, M. Ribo, and C. Puente, "Multiband handset antenna combining a PIFA, slots, and ground plane modes," *IEEE Trans. Antennas Propag.*, vol. 57, no. 9, pp. 2526–2533, Sep. 2009.

[44] S. Zhang, B. K. Lau, A. Sunesson, and S. He, "Closely-packed UWB MIMO/diversity antenna with different patterns and polarizations for USB dongle applications," *IEEE Trans. Antennas Propag.*, vol. 60, no. 9, pp. 4372–4380, Sep. 2012.

[45] S. Zhang, K. Zhao, Z. Ying, and S. He, "Investigation of diagonal antenna-chassis mode in mobile terminal LTE MIMO antennas for bandwidth enhancement," *IEEE Antennas Propag. Mag.*, vol. 57, no. 2, pp. 217–228, Apr. 2015.

[46] H. Li, Y. Tan, B. K. Lau, Z. Ying, and S. He, "Characteristic mode based tradeoff analysis of antenna-chassis interactions for multiple antenna terminals," *IEEE Trans. Antennas Propag.*, vol. 60, no. 2, pp. 490–502, Feb. 2012.

[47] Z. Miers, H. Li, and B. K. Lau, "Design of bandwidth-enhanced and multiband MIMO antennas using characteristic modes," *IEEE Antennas Wireless Propag. Lett.*, vol. 12, pp. 1696–1699, Nov. 2013.

[48] H. Li, Z. T. Miers, and B. K. Lau, "Design of orthogonal MIMO handset antennas based on characteristic mode manipulation at frequency bands below 1 GHz," *IEEE Trans. Antennas Propag.*, vol. 62, no. 5, pp. 2756–2766, May 2014.

[49] Y. Chen and C.-F. Wang, *Characteristic Modes: Theory and Applications in Antenna Engineering*, 1st ed. Hoboken, NJ, USA: Wiley, 2015.

[50] I. Papapolymerou, R. F. Drayton, and L. P. B. Katehi, "Micromachined patch antennas," *IEEE Trans. Antennas Propag.*, vol. 46, no. 2, pp. 275–283, Feb. 1998.

[51] Microwave Vision Group. *StarLab 50 GHz*. [Online]. Available: https://www.mvg-world.com/en/products/field_product_family/antenna-measurement-2/starlab-50-ghz

[52] Microwave Vision Group. *INSIGHT*. [Online]. Available: http://www.mvg-world.com/en/products/field_product_family/antenna-measurement-2/insight

[53] A. Razavi, A. A. Glazunov, P. S. Kildal, and J. Yang, "Characterizing polarization-MIMO antennas in random-LOS propagation channels," *IEEE Access*, vol. 4, pp. 10067–10075, 2016.

[54] W. Hong, "Solving the 5G mobile antenna puzzle: Assessing future directions for the 5G mobile antenna paradigm shift," *IEEE Microw. Mag.*, vol. 18, no. 7, pp. 86–102, Nov. 2017.

[55] D. Liu, X. Gu, C. W. Baks, and A. Valdes-Garcia, "Antenna-in-package design considerations for Ka-band 5G communication applications," *IEEE Trans. Antennas Propag.*, vol. 65, no. 12, pp. 6372–6379, Dec. 2017.

[56] O. M. Bucci and G. Franceschetti, "On the degrees of freedom of scattered fields," *IEEE Trans. Antennas Propag.*, vol. 37, no. 7, pp. 918–926, Jul. 1989.

[57] K. Persson and M. Gustafsson, "Reconstruction of equivalent currents using a near-field data transformation—With radome applications," *Prog. Electromagn. Res.*, vol. 54, pp. 179–198, 2005.

[58] J. L. A. Quijano and G. Vecchi, "Improved-accuracy source reconstruction on arbitrary 3-D surfaces," *IEEE Antennas Wireless Propag. Lett.*, vol. 8, pp. 1046–1049, 2009.

[59] K. Persson, M. Gustafsson, and G. Kristensson, "Reconstruction and visualization of equivalent currents on a radome using an integral representation formulation," *Prog. Electromagn. Res. B*, vol. 20, pp. 65–90, 2010.

[60] J. L. A. Quijano and G. Vecchi, "Field and source equivalence in source reconstruction on 3D surfaces," *Progr. Electromagn. Res.*, vol. 103, pp. 67–100, 2010.

[61] J. A. Quijano *et al.*, "3D spatial filtering applications in spherical near field antenna measurements," in *Proc. AMTA Symp.*, Atlanta, GA, USA, Oct. 2010.

[62] J. L. A. Quijano, L. Scialacqua, J. Zackrisson, L. J. Foged, M. Sabbadini, and G. Vecchi, "Suppression of undesired radiated fields based on equivalent currents reconstruction from measured data," *IEEE Antennas Wireless Propag. Lett.*, vol. 10, pp. 314–317, 2011.

[63] L. Scialacqua, L. J. Foged, F. Mioc, and F. Saccardi, "Link between measurement and simulation applied to antenna scattering and placement problems," in *Proc. 11th Eur. Conf. Antennas Propag. (EUCAP)*, Mar. 2017, pp. 2951–2955.

[64] T. Wu, T. S. Rappaport, and C. M. Collins, "Safe for generations to come: Considerations of safety for millimeter waves in wireless communications," *IEEE Microw. Mag.*, vol. 16, no. 2, pp. 65–84, Mar. 2015.

[65] D. Andreuccetti, R. Fossi, and C. Petrucci. (1997). An Internet resource for the calculation of the dielectric properties of body tissues in the frequency range 10 Hz–100 GHz. IFAC-CNR. Florence, Italy. [Online]. Available: http://niremf.ifac.cnr.it/tissprop/

[66] "Study on channel model for frequencies from 0.5 to 100 GHz," Eur. Telecommun. Standards Inst., Sophia Antipolis, France, Tech. Rep. 138 901, 3GPP TR 38.901 version 14.1.1 Release 14, Aug. 2017.

[67] W. Roh *et al.*, "Millimeter-wave beamforming as an enabling technology for 5G cellular communications: Theoretical feasibility and prototype results," *IEEE Commun. Mag.*, vol. 52, no. 2, pp. 106–113, Feb. 2014.

[68] "UE antenna array configuration for mmWave 28 GHz," 3GPP, Tech. Rep. R4-1704864, May 2017.

[69] K. F. Lee and K. M. Luk, *Microstrip Patch Antennas*. Singapore: World Scientific, 2011.

BO XU (S'14–M'18) received the B.E. degree in information engineering and the Ph.D. degree in optical engineering from Zhejiang University, Hangzhou, Zhejiang, China, in 2010 and 2017, respectively. He is currently pursuing the joint Ph.D. degree with the Department of Electromagnetic Engineering, KTH Royal Institute of Technology, Stockholm, Sweden, and the Centre for Optical and Electromagnetic Research, Zhejiang University. He was a Visiting Student with the Department of Electrical and Information Technology, Lund University, Lund, Sweden, from 2016 to 2017.

Since 2018, he has been an Experienced Researcher with Ericsson Research, Ericsson AB, Stockholm. His research interests include EMF health and safety, antenna design and measurement, and RFID.

ZHINONG YING (SM'05) is currently a Principle Engineer of antenna technology with the Network Technology Lab within the Research and Technology, Sony Mobile Communication AB, Lund, Sweden, and also as a Distinguish Engineer within the whole Sony group. He joined Ericsson AB in 1995. He became a Senior Specialist in 1997 and an Expert in 2003 in his engineer career at Ericsson. He has also been a Guest Professor with the Joint Research Centre, KTH Royal Institute of Technology, Sweden, and Zhejiang University, China, since 2001. He was a member of the Scientific Board of the Antenna Centre of Excellent in European 6th Frame program from 2004 to 2007. He served as TPC Co-Chairmen for the International Symposium on Antenna Technology, in 2007, and a Session Organizer of several international conferences, including the IEEE APS, and a reviewer for several academic journals.

He has authored and co-authored over 140 papers in various journal, conference, and industry publications. He holds over 147 patents and pending in the antennas and new generation wireless network areas. He contributed several book chapters on mobile antenna, small antenna, and MIMO antennas in *Mobile Antenna Handbook* (Third edition) edited by H. Fujimoto and the *Handbook of Antenna Technologies* edited by Z. N. Chen. He had contributed a lot of work in antenna designs and evaluation methods for the mobile industry. He has also involved in the evaluation of Bluetooth technology which was invented by Ericsson. His main research interests are small antennas, broad and multi-band antenna, multi-channel antenna (MIMO) system, antenna for body area network, antenna and propagation in the fifth generation mobile network, including massive MIMO and mmWave, near-field and human body effects and measurement techniques. He received the Best Invention Award at Ericsson Mobile in 1996 and the Key Performer Award at Sony Ericsson in 2002. He was nominated for the President Award at Sony Ericsson in 2004 for his innovative contributions. He received the Distinguish Engineer title at Sony Group globally in 2013.

LUCIA SCIALACQUA received the M.S. degree in telecommunication engineering from the University of Siena, Siena, Italy, in 2006.

She was a student under the Erasmus Program, Denmark Technical University, Lyngby, where she developed her master thesis on design of reference probes for near-field antenna measurements in 2006. In 2007, she joined MVG (formerly SATIMO) as an Antenna Engineer. In MVG, she worked initially as an antenna engineer for designing, testing of reference antennas and custom radiators under customer's specifications. She was a project manager of different projects involving antenna design and testing, antenna measurement, and measured data postprocessing. She is currently a Scientific SW Department Engineer, being technical responsible of the MVG software INSIGHT for measurement antenna post-processing, which uses the equivalent current reconstruction for antenna diagnostics and link with commercial numerical tools.

She has authored or co-authored over 80 journal and conference papers on antenna design and measurement topics and two white papers. She has contributed to one book. She was the speaker for three webinars on measurement antenna post-processing based on the equivalent current technique.

ALESSANDRO SCANNAVINI received the M.S. degree in electronic engineering from the Sapienza University of Rome, Rome, Italy, in 2000.

He was with the Motorola Design Center, Turin, Italy, and Chicago, IL, USA, from 2000 to 2006. He was involved in designing antenna and RF components for 2G and 3G products. In 2007, he joined the Microwave Vision Group (MVG) as a Field Application Engineer. In MVG, he worked with the research and development team on new technologies to be used for designing accurate and fast antenna measurement systems and was involved in pre-sale and after sale activities. In 2009, he initiated his new role in representing MVG in standardization bodies, such as 3G Partnership Project (3GPP) and CTIA-The Wireless Industry. He is currently the Standardization Specialist of the MVG. He actively contributed to the MIMO OTA test plan, and the 3GPP AAS BS OTA specifications with authoring and co-authoring over 50 contributions. He is involved in 5G solutions for OTA measurements at sub 6 GHz and mmWave and actively contributing to the standard for NR UE conformance testing.

LARS JACOB FOGED (M'91–SM'00) received the B.S. degree from Aarhus Teknikum, Denmark, in 1988, and the M.S. degree in electrical engineering from California Institute of Technology, USA, in 1990.

He was a Graduate Trainee with the European Space Agency, ESTEC, and in the following 10 years, he designed communication and navigation antennas in the satellite industry. He led the antenna design effort on the recently launched GALILEO space segment and performed the multi-physics design of shaped reflectors for the EUTELSAT W satellites, still serving European users. Following his passion to rationalize the multi-disciplinary antenna design process, including measurements and simulations, he joined the Microwave Vision Group (MVG) in 2001 and founded the Italian branch office. In MVG, he initiated close collaborations with universities and research institutions on measurements with focus on antennas and techniques for analysis/postprocessing. He has held different technical leadership positions at MVG, where he is currently the Scientific Director. He is also an Associate Director of Microwave Vision Italy. He contributed to the European network of excellence "ACE" as an Activity Leader on "Antenna Measurements and Facility Sharing" from 2004 to 2008. He was a member of the EURAAP Delegate Assembly and responsible for the Working Group on Antenna Measurements from 2009 to 2012. He was the Vice-Chair of the EUCAP Conference in 2011, the Industrial Chair of EUCAP Conference in 2012, 2014, and 2017, respectively, and the Technical Program Chair of EUCAP in 2016. In 2015, he contributed to the foundation of the AMTA Italian node.

He has authored or co-authored over 200 journal and conference papers on antenna design and measurement topics. He has contributed to five books and standards, and holds four patents. Since 2004, he has been a Secretary of the IEEE Antenna Standards Committee and has contributed to the development of different standards on antennas and measurements. He has been a Board Member of the European School of Antennas and a technical responsible and teacher in antenna measurement courses in Europe and Asia since 2006. He has been involved in the evolution of the IEC standards on human exposure to electromagnetic fields since 2010. In 2016 and 2017, he led the Industry Initiatives Committee, a standing committee of the IEEE APS. He is an Edmond S. Gillespie Fellow of AMTA. He received the Best Technical Paper Award from AMTA in 2013 and the Distinguished Achievement Award from AMTA in 2017.

THOMAS BOLIN received the M.Sc. degree in applied physics and electrical engineering from Linköping University, Sweden, in 1979.

From 1979 to 1983, he held an RF-development engineer position at ITT Standard Radio and Telefon AB, Stockholm, doing 1-kW HF PA and filter designs. From 1983 to 2001, he held a technical management position at Ericsson Mobile Communications, Lund, Sweden, doing RF and antenna product development and the OTA measurement technology development for mobile handsets. From 2001 to 2011, he held a technical management position at Sony Ericsson Mobile Communications, Lund. Since 2011, he has been with Sony Mobile Communications AB, Lund, where he is currently more devoted to antenna research and standardization. Frequently, he was a 3GPP RAN 4 delegate. He assisted in the development of mm-wave antenna arrays and FEM integration (15–40 GHz) for 5G.

SAILING HE (M'92–SM'98–F'13) received the Licentiate of technology and Ph.D. degrees in electromagnetic theory from the KTH Royal Institute of Technology (KTH), Stockholm, Sweden, in 1991 and 1992, respectively. Since then, he has worked at the same division of the KTH Royal Institute of Technology as an Assistant Professor, an Associate Professor, and a Full Professor. He also serves as the Director for a joint research center between KTH and Zhejiang University, China. His current research interests include applied electromagnetics, electromagnetic metamaterials, optoelectronics, microwave photonics, and biomedical applications. He has first-authored one monograph (Oxford University Press) and authored/co-authored about 500 papers in refereed international journals. He has served in the leadership for many international conferences. He has given many invited/plenary talks in international conferences.

KUN ZHAO received the B.S. degree in communication engineering from the Beijing University of Posts and Telecommunications, Beijing, China, in 2010, the M.S. and Ph.D. degree from KTH Royal Institute of Technology, Stockholm, Sweden, in 2012 and 2017, respectively.

He is currently a Researcher of antenna technology with the Network Research Lab within the Technology Office, Sony Mobile Communication AB, Lund, Sweden. He has been a Visiting Researcher with the Department of Electrical and Information Technology, Lund University, Sweden. His current research interests include mm-wave antenna and propagation for 5G communications, MIMO antenna systems, user body interactions, and body centric wireless communications.

MATS GUSTAFSSON (M'05–SM'17) received the M.Sc. degree in engineering physics and the Ph.D. degree in electromagnetic theory from Lund University, Sweden, in 1994 and 2000, respectively.

In 2005, he was the Docent with Lund University, where he was a Professor of electromagnetic theory in 2011. He co-founded the company Phase Holographic Imaging AB in 2004. He has authored or co-authored over 90 peer-reviewed journal papers and over 100 conference papers. His research interests are in scattering and antenna theory and inverse scattering and imaging with applications in microwave tomography and digital holography.

Dr. Gustafsson received the Best Antenna Poster Prize from EuCAP 2007, the IEEE Schelkunoff Transactions Prize Paper Award 2010, and the Best Antenna Theory Paper Award from EuCAP 2013. He served as an IEEE AP-S Distinguished Lecturer from 2013 to 2015.

• • •